

The Vela and Geminga pulsars in the mid-infrared

A. A. Danilenko,^{1*} D. A. Zyuzin,^{1,2} Yu. A. Shibano^{1,2} and S. V. Zharikov³

¹*Ioffe Physical Technical Institute, Politekhnikeskaya 26, St. Petersburg, 194021, Russia*

²*St. Petersburg State Polytechnical Univ., Politekhnikeskaya 29, St. Petersburg, 195251, Russia*

³*Observatorio Astronómico Nacional SPM, Instituto de Astronomía, UNAM, Ensenada, BC, Mexico*

Accepted by MNRAS 2011 March 20. Received 2011 March 14; in original form 2010 October 8

ABSTRACT

The Vela and Geminga pulsars are rotation powered neutron stars, which have been identified in various spectral domains, from the near-infrared to hard γ -rays. In the near-infrared they exhibit tentative emission excesses, as compared to the optical range. To check whether these features are real, we analysed archival mid-infrared broadband images obtained with the *Spitzer* Space Telescope in the 3.6–160 μm range and compared them with the data in other spectral domains. In the 3.6 and 5.8 μm bands we detected at $\sim (4\text{--}5)\sigma$ significance level a point-like object, that is likely to be the counterpart of the Vela pulsar. Its position coincides with the pulsar at $\lesssim 0''.4$ 1σ -accuracy level. Combining the measured fluxes with the available multiwavelength spectrum of the pulsar shows a steep flux increase towards the infrared, confirming the reality of the near-infrared excess reported early, and, hence, the reality of the suggested mid-infrared pulsar identification. Geminga is also identified, but only at a marginal 2σ detection level in one 3.6 μm band. This needs a farther confirmation by deeper observations, while the estimated flux is also compatible with the near-infrared Geminga excess. The detection of the infrared excess is in contrast to the Crab pulsar, where it is absent, but is similar to the two magnetars, 4U 0142+61 and 1E 2259+586, showing similar features. We discuss X-ray irradiated fall-back discs around the pulsars, unresolved pulsar nebula structures, and pulsar magnetospheres as possible origins of the excesses. We note also possible infrared signatures of an extended tail behind Geminga and of the Vela plerion radio lobes.

Key words: infrared: stars – stars: neutron – pulsars: the Vela and Geminga pulsars.

1 INTRODUCTION

The two nearby middle-aged pulsars, Vela (PSR B0833–45) and Geminga (PSR J0633+1746), belong to a small group of rotation powered neutron stars (NSs), which are identified in various spectral domains outside the radio range. Both pulsars have counterparts in the near-infrared (IR) and optical (e.g., Shibano et al. 2003, 2006; Mignani, Zharikov & Caraveo 2007, and references therein), in the ultraviolet (UV) (Romani, Kargaltsev & Pavlov 2005; Kargaltsev et al. 2005), soft X-rays (e.g., Pavlov et al. 2001; Kargaltsev et al. 2005; Caraveo et al. 2004, and references therein), hard X-rays (Harding et al. 2002), and γ -rays (Abdo et al. 2010a,b, and references therein). Emission mechanisms of pulsars are still poorly understood, and the presence of such multiwavelength objects is very useful for the progress in this field.

In soft X-rays and extremal ultraviolet (EUV) the emis-

sion from the Vela and Geminga pulsars is dominated by the thermal blackbody (BB) like radiation believed to be originated from cooling surfaces of the NSs, and, possible, from their hot polar caps. In the rest ranges the spectra are described by a power-law (PL) with different spectral indices in different spectral domains. This emission is nonthermal and generated by relativistic particles accelerated in magnetospheres of the rapidly rotating and strongly magnetized NSs.

In the optical the nonthermal spectra of both pulsars are significantly flatter than in soft X-rays, and the optical fluxes are considerably below the long wavelength extrapolations of their nonthermal X-ray spectra. This suggests a spectral break between the two ranges. Similar spectral picture is observed for the young Crab pulsar. In the near-IR the Vela and Geminga pulsars exhibit apparent flux excesses, as compared to the optical range (Shibano et al. 2003, 2006). This is in contrast to the Crab, whose near and mid-IR fluxes are compatible with the spectral extrapolation from the optical range (Sandberg & Sollerman 2009; Temim et al. 2009). The near-IR excesses appear to increase

* E-mail: danila@astro.ioffe.ru

Table 1. *Spitzer* observations of the Vela and Geminga pulsars.

| AOR key | Dev. | Obs. date, yy/mm/dd | Channels, μm | Int. time ^a , s |
|-----------------------|------|------------------------|----------------------------|-------------------------------|
| the Vela pulsar | | | | |
| 11374848 ^b | IRAC | 04/12/17 | 3.6, 5.8, | 72 |
| - | - | - | 4.5, 8.0 | 72 |
| 11375104 ^b | MIPS | 05/03/07 | 24 | 92 |
| - | - | - | 70 | 335 |
| - | - | - | 160 | 105 |
| 11542784 ^c | IRAC | 04/12/18 | 3.6, 5.8 | 9400 |
| the Geminga pulsar | | | | |
| 12540928 ^d | MIPS | 05/04/04 | 24 | 501 |
| 12543232 ^d | IRAC | 05/03/26 | 3.6, 5.8, | 270 |
| - | - | - | 4.5, 8.0 | 270 |
| 19037696 ^e | IRAC | 06/10/30 | 3.6, 5.8 | 14700 |
| 19037952 ^e | IRAC | 06/11/22 | 3.6, 5.8 | 14700 |

^a The integration time shown for the IRAC is the same for the each channel in a given AOR

^b PI, Patrick O. Slane, Program ID = 3647

^c PI, Divas Sanwal, Program ID = 3696

^d PI, Michael Jura, Program ID = 23

^e PI, Deepto Chakrabarty, Program ID = 30822

with the wavelength, and mid-IR observations can be useful to confirm or discard their reality.

Besides the Crab pulsar, there are only two isolated NSs detected in the mid-IR. Both are anomalous X-ray pulsars (AXPs), 4U 0142+61 and 1E 2259+586. A strong mid-IR flux excess was observed for the first one (Wang, Chakrabarty & Kaplan 2006), and similar, but less evident feature was found for the second (Kaplan et al. 2009). The excesses can be interpreted as signatures of the so-called fall-back discs which can be formed around NSs shortly after the supernova (SN) explosions. Such discs can be progenitors of pulsar planetary systems, one of which was discovered around PSR B1257+12 (Wolszczan 1994; Konacki & Wolszczan 2003). However, the association of the excesses with the intrinsic pulsar emission still can not be excluded.

In addition to their multiwavelength emission, the Vela and Geminga pulsars power extended pulsar wind nebulae (PWNe) most clearly visible in soft X-rays (Helfand, Gotthelf & Halpern 2001; Pavlov et al. 2001a; Caraveo et al. 2003; de Luca et al. 2006; Pavlov, Sanwal & Zavlin 2006; Pavlov, Bhattacharyya & Zavlin 2010). The PWN morphologies are different. The younger Vela ($\sim 10^4$ yr old) is associated with the supernova remnant (SNR) G263.9–3.3 and, as the Crab pulsar, forms a torus-like inner PWN with polar jets. The PWN of the older Geminga ($\sim 3.4 \times 10^5$ yr) has a tail and/or a bow-shock morphology. At larger spatial scales the Vela PWN has a cocoon, or a plerion, structure. It is mainly elongated southwards the pulsar, that is roughly orthogonal to the orientation of the inner PWN symmetry axis (Markwardt & Ogelman 1995; Dodson et al. 2003a). The cocoon has been detected in the GeV range with *Fermi* (Abdo et al. 2010c) and the AGILE (Pellizzoni et al. 2010), and in the TeV range with the HESS (Aharonian et al. 2006). It is speculated, that

the high energy source may be a 'relict' PWN distorted by the passage of the remnant reverse shock in inhomogeneous medium (Blondin, Chevalier & Frierson 2001). Geminga is not associated with any SNR, although, it is discussed (Salvati 2010), that a dissolved and not visible Geminga SNR could be a plausible source of a small scale excess in multi-TeV cosmic ray protons arrival direction (spot A) discovered with Milagro (Abdo et al. 2008).

Both PWNe have no obvious optical counterparts. Some faint extended features were detected in the near-IR with the VLT in the $1''.5$ – $3''.1$ vicinity of the Vela pulsar (Shibanov et al. 2003). They are projected on and/or aligned with the south-east jet and the inner arc of its X-ray PWN. There is also a faint optical nebulosity with a size of few arcsec around the Geminga pulsar detected in a deepest up to date optical image obtained in the *I* band with the Subaru telescope (Shibanov et al. 2006). The nebula is extended perpendicular of the pulsar proper motion, and, probably, is the brightest inner part of the bow-shock structure which is seen in X-rays. However, the PWN origin of those features still needs to be confirmed.

Motivated by further studies of the IR flux excesses in the emission of both pulsars and by searching for their PWN IR-counterparts, in this paper we analyse unpublished archival mid-IR images of the pulsar fields obtained with the *Spitzer* Space Telescope. We report on finding likely mid-IR counterparts of the pulsars and possible features of their PWNe. The mid-IR observations are described in Sect. 2, the results are presented and discussed in Sect. 3 and 4.

2 OBSERVATIONS AND DATA ANALYSIS

2.1 *Spitzer* data

The Vela and Geminga pulsar fields have been imaged several times with the *Spitzer* telescope using the Infrared Array Camera (IRAC) and the Multiband Imaging Photometer for *Spitzer* (MIPS)¹. Various instrument channels have been used with the effective wavelengths of 3.6, 4.5, 5.8, 8, 24, 70, and 160 μm . The information on the respective Astronomical Observation Requests (AORs) is presented in Table 1. We retrieved the data from the *Spitzer* archive. We used the IRAC post-BCD (Best Calibrated Data) mosaic images with an effective image scale of $0''.6$ per pixel and the field of view (FOV) of $7''.5 \times 7''.5$. They have been generated with the *Spitzer* pipeline procession version of S18.7.0. We also regenerated the MIPS post-BCD calibrated mosaic images from respective BCD data using the MOPEX² tool v18.3.1. The resulting image scales are $2''.4$ per pixel for the 24 μm MIPS channel with the FOV of $13''.3 \times 12''.8$. After the pipeline drizzling of multiple individual exposures the effective pixel scale for the IRAC mosaics is twice smaller than the nominal one ($1''.2$ per pixel), while for the MIPS it is consistent with the nominal pixel scale of $2''.4$.

First inspections of the archival data showed that a point-like counterpart candidate of the Vela pulsar is detected at $\gtrsim 4\sigma$ significance level in the 3.6 and 5.8 μm images of the AOR 11542784, where the integration time was

¹ see <http://ssc.spitzer.caltech.edu>

² see <http://ssc.spitzer.caltech.edu/postbcd/mopex.html>

maximal among the other AORs for this target (cf. Table 1). The respective mosaic coverage maps show that the real integration times of the pulsar neighbourhood located in the centre of the mosaic images are only 1–3 % smaller than the AOR nominal archival integration time shown in Table 1. At the shorter AOR 11374848 the source is probably marginally detected at 3.6, 4.5, and 5.8 μm , and it is not detected at 8 μm . A bright pixel at the source position is seen in the 24 μm image (AOR 11375104), while at longer wavelengths no signatures of the pulsar are detected.

A likely counterpart of the Geminga pulsar is marginally detected at $\sim 2\sigma$ significance level in the 3.6 μm images of the long integration time AORs 19037696 and 19037952. These AORs differ by a zodiacal background level, that was ~ 30 % smaller in the second AOR. At 5.8 μm the candidate is not resolved even in the image combined from the data of the two AORs. However, we found some sign of it in the 4.5 μm image of the shorter AOR 12543232. In other *Spitzer* bands and shorter AORs we have not found any signature of the pulsar.

To check that the detected counterpart candidates are not the detector artefacts or results of a poor cosmic ray rejection, we analysed the respective badpixel masks, provided by the archive together with the data, and regenerated the mosaic images from the BCD data using the MOPEX tool v18.3.1. We used the nominal IRAC pixel scale and a half of it, as has been done in the pipeline processed images discussed above. For the Vela AORs we obtained the similar results, confirming the reality of the counterpart candidate detection in both IRAC bands of the AOR 11542784 and the presence of a bright pixel at the source position in the 24 μm image of the AOR 11375104. There is a bright star located in 0'.5 north-east of the Vela pulsar. In 3.6 and 5.8 μm images it is oversaturated and produces typical stray light artefacts. However, the nearest one is in ~ 8 arcsec south-east of the pulsar position and cannot induce a false source detection at least in a few arcsec region around the pulsar. The marginal Geminga counterpart in 3.6 μm images of the AORs 19037696 and 19037952 was found to be present at the same significance level in the nominal and the half pixel scale regenerated mosaics. However, at the 4.5 μm it disappears in the nominal pixel scale mosaic. Its apparent presence in the half pixel scale drizzled mosaic is likely to be an artificial background fluctuation resulting from an inappropriate use of the 0''.6 pixel scale in the pipeline data procession for a shallow observation in this band, where only nine separate exposures have been obtained. Therefore, only an upper limit on the Geminga flux can be set in this band. Further investigation of the 3.6 μm images of Geminga showed that they contain some artefacts. These are so called 'muxbleed' and 'muxstripes', which are due to the presence of two bright stars in the FOV north-west of Geminga and which cannot be perfectly corrected by the reduction tool at given AOR setups³. The respective stripes cross the whole mosaics from north to south approximately. However, the nearest one is located in $\sim 0'.5$ west of the Geminga position and cannot result in a false source detection, at least in several tenths arcsec pulsar neighbourhoods.

Thus, we can conclude, that the Vela counterpart candidate in the 3.6 and 5.8 μm images is definitely the real source. The Geminga candidate in 3.6 μm images is likely to be the real source as well, but it is much fainter and detected at a lower significance level. The source reality is additionally supported by its independent detection at about the same significance level in the two AORs, which were obtained at different epochs and conditions. Below we mainly focus on the data where our counterpart candidates have been checked to be the real mid-IR sources.

2.2 Astrometry

The coordinates and proper motions of the Vela and Geminga pulsars are known with a high accuracy based on the radio and optical observations (Caraveo et al. 2001; Dodson et al. 2003; Bignami, Caraveo & Mereghetti 1993; Faherty, Walter & Anderson 2007). For correct positional identifications of the pulsars with the sources detected in the mid-IR, one has to be sure in the *Spitzer* pointing accuracy. To check this in the IRAC images of both pulsars, we selected about two dozens of unsaturated isolated astrometric standards from the USNO-B1 catalogue. Their catalogue and image positional uncertainties for both coordinates were $\lesssim 0''.2$ and $\lesssim 0''.5$, respectively. IRAF *ccmap/cctran* tasks were used to find plate solutions. Formal rms uncertainties of the astrometric fit were $\lesssim 0''.16$ with maximal residuals of $\lesssim 0''.4$ for both coordinates. After astrometric transformations the shifts between the original and transformed images were $\lesssim 0''.4$ for the Vela and $\lesssim 0''.2$ for the Geminga fields. This is less than the nominal pixel scale (1''.2) of the IRAC, ensuring the almost perfect pointing accuracy of the *Spitzer* observations. Combining all uncertainties, a conservative estimate of the 1σ referencing uncertainty is $\lesssim 0''.4$ in both coordinates for all IRAC images in question. This is comparable with astrometric uncertainties of available *Chandra*/ACIS and HRC images of the same fields in X-rays, but about twice as poor as for optical and near-IR images obtained with large ground based telescopes and the *HST*. Nevertheless, this allows us to identify positionally on a subarcsecond accuracy level the mid-IR, near-IR, optical and X-rays objects in the respective pulsar frames, which have been obtained with significantly different spatial resolutions and pixel scales.

3 RESULTS

3.1 Morphology of the Vela field

3.1.1 Identification of the Vela pulsar

In Fig. 1 we compare fragments of the 3.6 and 5.8 μm *Spitzer* images containing the Vela pulsar with the *J* and *H* band images of the same field obtained with the VLT/ISAAC in the period of December 2000 – January 2001 (Shibanov et al. 2003). The point-like near-IR pulsar counterpart is marked by a thick line, and it is clearly visible near the same position in the mid-IR. The measured coordinates of the counterpart candidate in the 3.6 μm image, where it is detected with a higher significance than at 5.8 μm , are $\text{RA}=08^{\text{h}} 35^{\text{m}} 20^{\text{s}}.635 \pm 0^{\text{s}}.042$ and $\text{Dec}=-45^{\circ}$

³ For details, see, e.g., the IRAC Instrument Handbook, <http://ssc.spitzer.caltech.edu/irac/iracinstrumenthandbook/>

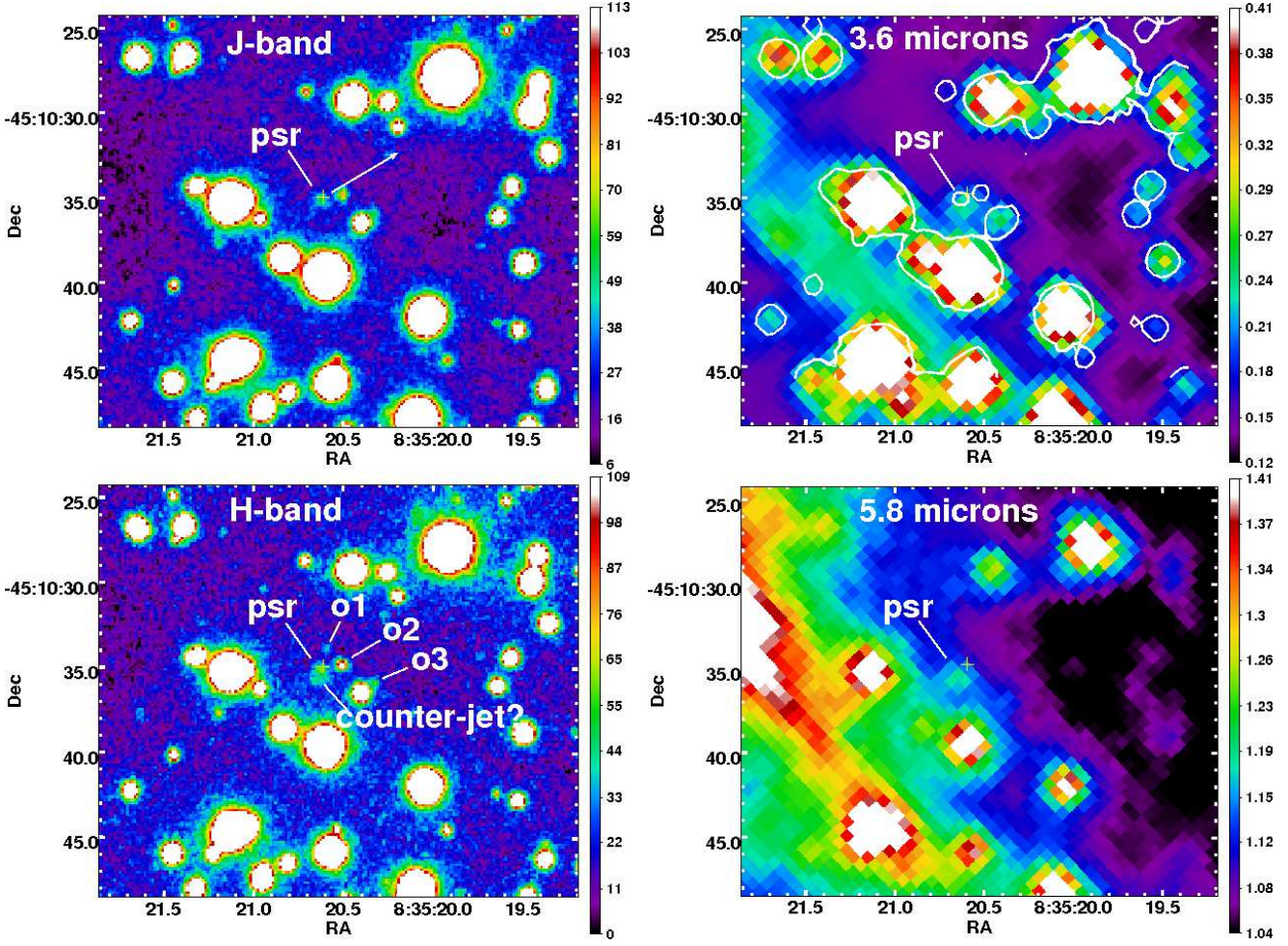


Figure 1. The $\sim 20'' \times 25''$ fragments of the infrared images of the Vela field obtained with the VLT/ISAAC in the *J* and *H* bands (left column), and with the *Spitzer*/IRAC (AOR 11542784) in 3.6 and 5.8 μm bands (right column). The Vela pulsar counterpart is marked by a thick line and the arrow shows the direction of its proper motion. Crosses are the expected pulsar radio positions defined separately for the VLT and *Spitzer* observation epochs. A knot-like object 'o1', an extended feature SE of the pulsar, possible associated with the X-ray PWN jet and counter-jet, and two background stars 'o2' and 'o3' are notified in the *H* band image. The contours in the 3.6 μm images are from the *J* band image. Henceforth the image pixel value scale is linear.

$10^\circ 35' 48 \pm 0' 45$ (J2000). The errors account for $\approx 0' 12$ object position uncertainties in the image and the mid-IR astrometric referencing uncertainties estimated in Sect. 2.2. Within 1σ the coordinates are consistent with the position of the near-IR counterpart, $\text{RA} = 08^{\text{h}} 35^{\text{m}} 20^{\text{s}} .628 \pm 0^{\text{s}} .01$ and $\text{Dec} = -45^\circ 10' 35'' 16 \pm 0' 1$ (J2000), which is defined with a higher accuracy due to a better spatial resolution of the VLT observations obtained with the pixel scale of $0' 147$. The contours overlaid on the 3.6 μm image from the *J* band image underline the positional consistency of the detected mid-IR candidate and the near-IR counterpart. They show also that all background near-IR sources, except of the two faint near-IR point-like objects 'o1' and 'o2' located in immediate vicinity north-west of the pulsar, are identified in the mid-IR and vice versa. Hence, the appearance of a new mid-IR background source at the pulsar position, not visible in the adjacent near-IR band, is very improbable. An apparent emission region extended from north-east to south-west in ~ 8 arcsec south-east of the pulsar is the stray light artefact from a bright saturated star located in $\sim 0' 5$ north-east of the presented frames. This has been mentioned in

Sect. 2.1 and may somewhat increase the backgrounds level near the pulsar position and decrease the significance of the candidate detection.

The pulsar proper motion is $\mu = 58 \pm 0.1$ mas yr^{-1} with a positional angle of $301^\circ 0 \pm 1^\circ 8$ (Dodson et al. 2003). Hence, the pulsar shift during four years between the VLT and *Spitzer* observation epochs is $\approx 0' 23$, that is indistinguishable within the derived positional error budget. Attempting to improve the accuracy of the positional identification we have performed the relative astrometry. The VLT *H* band image with a point-source FWHM $\approx 0' 5$ was used as a reference for finding the plate solution for the 3.6 μm image with FWHM $\approx 1' 8$. The IRAF *geomap/geoxytran* tool with a *general* geometry option, allowing for the image shifting, rotation, pixel scaling, and a skew, was applied. A dozen of unsaturated isolated stars, which are common for both frames and are located in vicinity of the pulsar, were selected as reference points. The formal rms uncertainties of the plate solution fit were $\lesssim 0' 09$ with maximal residuals of $\lesssim 0' 17$ for both image coordinates. The pixel scale ratio was ≈ 0.245 , that coincides with the nominal one for the two images. Us-

ing this solution we transformed the $3.6\ \mu\text{m}$ image coordinates of the mid-IR counterpart candidate to the H image. As a result, we obtained that the candidate counterpart is apparently displaced by $0''.41 \pm 0''.21$ to the south from the near-IR pulsar counterpart. Similar displacement can be noticed also from absolute astrometry results, which have been used in Fig. 1, where the mid-IR candidate position in the $3.6\ \mu\text{m}$ image is also slightly shifted toward the south from the near-IR pulsar contour. In any case, the shift significance is too small, $\lesssim 2\sigma$, to consider it seriously as a real one. Nevertheless, this may be a signature of a systematic shift caused by a faint extended feature located in the immediate vicinity southward of the pulsar and marked as a 'counter-jet' in the H band panel of Fig. 1. The feature is likely associated with the pulsar PWN and is clearly detected in the near-IR (Shibanov et al. 2003), but it cannot be resolved from the point source in the mid-IR due to a poor Spitzer spatial resolution. We shall discuss the implications of that later in Sect. 4.1.2. Using the plate solution and absolute astrometry of the H band image, we obtain the candidate coordinates, $\text{RA}=08^{\text{h}}\ 35^{\text{m}}\ 20^{\text{s}}.626 \pm 0^{\text{s}}.025$ and $\text{Dec}=-45^{\circ}\ 10'\ 35''.51 \pm 0''.26$ (J2000), which are consistent with those obtained from the direct mid-IR absolute astrometry, while they are formally about twice more accurate than the latter ones. However, these improvements do not still allow us to distinguish the counterpart proper motion. The new formal position error budget is still comparable with the proper motion shift of the pulsar, and including the possible systematic shift discussed above increases the positional uncertainties to the values obtained early from the absolute astrometry.

The expected radio coordinates of the pulsar at the mid-IR observation epoch are $\text{RA}=08^{\text{h}}\ 35^{\text{m}}\ 20^{\text{s}}.588 \pm 0^{\text{s}}.038$ and $\text{Dec}=-45^{\circ}\ 10'\ 34''.727 \pm 0''.4$ (J2000). They are derived from the most accurate VLBI radio position and proper motion measurements (Dodson et al. 2003), and the errors are dominated by the mid-IR astrometric referencing uncertainties. The displacement between the expected position and the mid-IR candidate centre is $\sim 0''.9$, or about $(2-3)\sigma$ of the coordinate uncertainty level. This can be resolved in Fig. 1, where radio positions are marked by crosses. The direction of the offset approximately coincides with the pulsar proper motion positional angle. Considering available optical/near-IR images obtained early with the VLT and *HST* and referenced with the USNO catalogue we got similar results: the expected radio positions are always marginally shifted by about $0''.2-0''.4$ ahead of the counterpart positions approximately along the line of the pulsar proper motion (cf. Fig. 1). The variation of the offset values can be explained by different spatial resolution of the observations, while the same direction of the offsets is noticeable. At the same time, the relative values, such as the counterpart motion and its shifts from one epoch to others, are compatible with the radio proper motion. Dodson et al. (2003) have discussed that some differences between the radio and optical absolute astrometries of the pulsar can be due to different astrometric standards used in the two ranges, i.e., very accurately established extragalactic standards in the radio and mainly Galactic standards in the optical, where proper motions are sometimes poorly known. Therefore, the apparent offsets of the optical/IR counterpart from the radio position of the pulsar are likely caused by unknown systematic uncertainty of the optical astrometric standards for the Vela field.

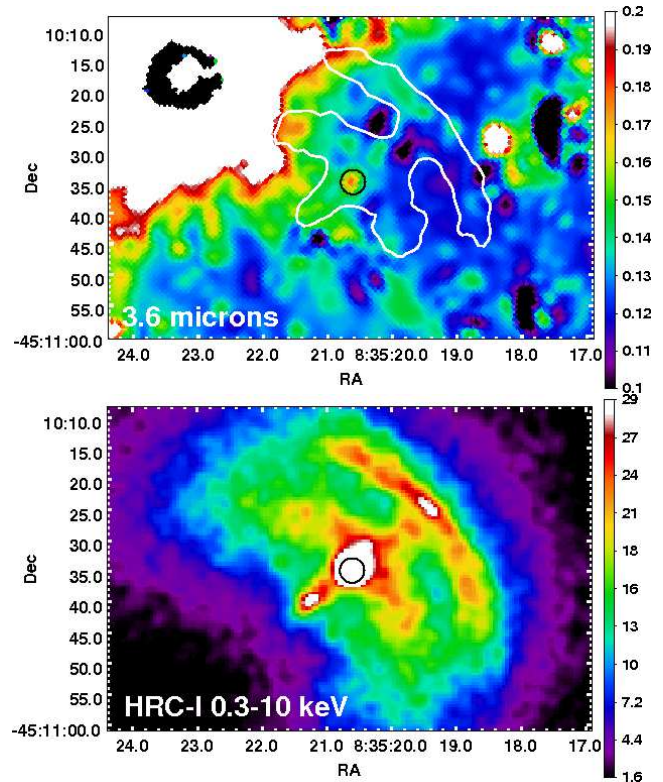


Figure 2. The $\sim 50'' \times 85''$ fragments of the star-subtracted $3.6\ \mu\text{m}$ (top) and the X-ray (bottom) images obtained with the *Spitzer*/IRAC (AOR 11542784) and *Chandra*/HRC-I, containing the Vela pulsar and the brightest part of its torus-like PWN. The circle marks the pulsar position. The contour indicating the position of the two bright arcs and south-east jet of the X-ray PWN at the bottom panel is overlaid on the mid-IR image.

Summarizing this part, the optical/near-IR counterpart of the Vela pulsar is firmly established based on its peculiar spectrum, proper motion, and pulsations with the pulsar period. Therefore, the 1σ agreement of the mid-IR counterpart candidate position with the near-IR counterpart coordinates, obtained by us using both the relative and absolute astrometries⁴, allows us to ignore the radio-optical standard systematics discussed above, and to conclude that the source detected in the two IRAC bands is likely to be associated with the pulsar. To confirm the identification by the mid-IR source proper motion measurements, higher spatial resolution and/or new *Spitzer* mid-IR observations at later epochs are necessary.

3.1.2 Searching for the Vela PWN

Immediate pulsar vicinity.

Previous attempts to find any optical counterpart of the Vela PWN have been unsuccessful (Mignani et al. 2003). In the near-IR H band image of Fig. 1 one can resolve a nearby knot-like source 'o1' north-west of the pulsar and a faint structure, 'counter-jet', extended by a few arcsec just south-east of the pulsar (Shibanov et al. 2003). Both are projected

⁴ We got the same results considering another available optical images of different epochs as reference frames.

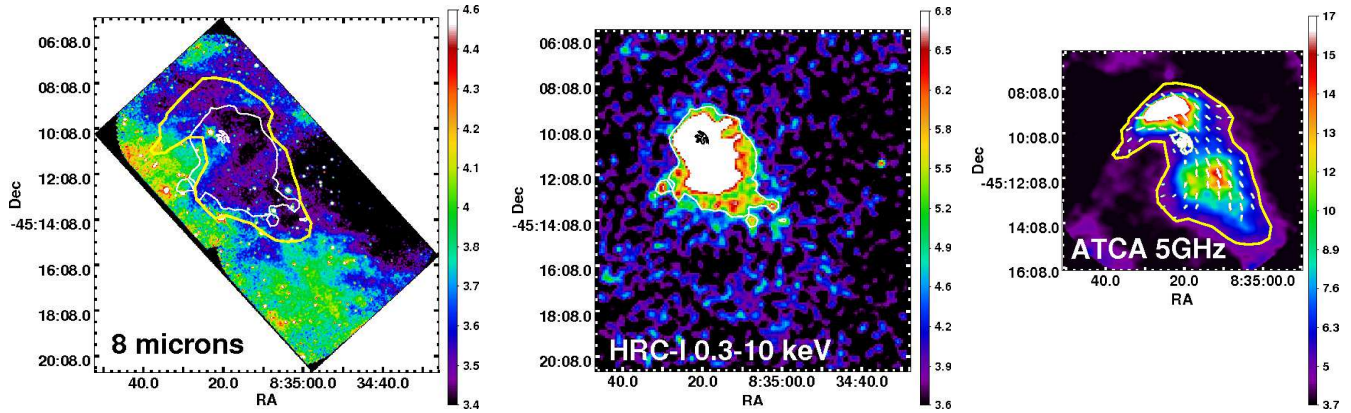


Figure 3. The large-scale structure of the Vela plerion at 5 GHz, 8 μ m, and in soft X-rays, as seen with the ATCA (right (Dodson et al. 2003a)), *Spitzer*/IRAC (AOR 11374848) (left), and *Chandra*/HRC-I (middle). The contours in the 8 μ m image are from the 5 GHz and X-ray images. The central black and white contours in the X-ray and radio/mid-IR images indicate the location of the internal torus-like structure of the PWN zoomed in Fig. 2. Ticks in the 5 GHz image show magnetic field lines.

on the pulsar X-ray jet/counter-jet structures, and may be associated with the PWN. We do not detect them in the mid-IR. A possible reason is that the second structure can be hidden in the pulsar-candidate source wings due to a lower spatial resolution of the *Spitzer*/IRAC as compared to the VLT/ISAAC (see Sect. 3.1.1). The more distant knot could be resolved, however it is not detected. It is also not visible in any available optical images obtained at different epochs. If it is not an artefact, it may be a time variable source.

To search for PWN structures at larger scales, we performed PSF subtraction of background stars from the *Spitzer* images making use of the IRAF *daophot/allstar* tool. The results for the brightest inner torus-like part of the PWN are shown in Fig. 2, where we compare the star-subtracted 3.6 μ m image with the archival *Chandra*/HRC-I X-ray image⁵. The pulsar counterpart candidate was not subtracted and its position is compatible with the X-ray position of the pulsar marked by the circle. Some remains of a poorly subtracted saturated field stars are visible, but no counterparts of the X-ray torus-like structure with jets and arcs are detected. We have not found them in other *Spitzer* bands as well.

Plerion.

The inner torus-like PWN, shown in Fig. 2, is only a tiny part of the Vela plerion, that extends in the radio and X-rays to several arcminutes. The respective field is shown in Fig. 3, where we compare the 8 μ m, soft X-ray, and 5 GHz images. We reproduced the 5 GHz image from fig. 10 of Dodson et al. (2003a). To reveal the plerion X-ray structure the *Chandra*/HRC-I image is binned by 16 pixels and smoothed with 3 pixel Gaussian kernel. The image intensity scale is also different, as compared to that of Fig. 2, to reveal fainter emission from outer PWN regions, while its inner torus-like part is indicated by the contour taken from Fig. 2 to demonstrate its small extent as compared to the whole plerion size. We have applied contours from the 5 GHz and X-ray images on the 8 μ m image. Contour taken from

the X-ray image shows the outer boundary of the X-ray plerion, where it merges with backgrounds, as it is seen with the HRC. Contour taken from the 5 GHz image indicate the outer boundary of the radio plerion, which consists of two bright, the north and south, radio ‘lobes’, located symmetrically with respect to the inner PWN symmetry axis. The inner PWN X-ray contours are overlaid on the 5 GHz image, though this part of the PWN is not detected in the radio range. In contrast to the torus-like structure, whose symmetry axis is directed north-west approximately along the proper motion of the pulsar, the plerion is mainly extended south-west.

As well as in the radio image, the pulsar and its inner PWN are not detected at 8 μ m. However, the outermost east boundary of the large scale plerion and its south-west extension in the radio and X-rays likely correlate with the west boundary of a bright extended emission structure in the mid-IR, which also extends south-west and, possible, originates from the dust formed from the remnant ejecta and heated by the PWN. In other SNRs at longer wavelengths the radiation from such extended structures is typically dominated by continuum emission from the dust, that can significantly contribute to the radiation of a remnant at 8 μ m as well (see, e.g., Rho et al. 2009). Indeed, the similar but brighter structure is visible at 24 and 70 μ m images obtained with the MIPS. However, they have much smaller and not representative FOVs, and we do not show them here. Nevertheless, the fact, that the extended mid-IR emission is visible in the images obtained with different *Spitzer* detectors in three different bands, at different AORs and observation conditions, suggests that it is real, but not a result of an artificial background variation. At shorter wavelengths the extended emission disappears, as expected for a rather cold dust.

The centre of the associated with the plerion TeV source HESS J0855–455 (Aharonian et al. 2006) is located tens arcminutes south-west and is outside the frames shown in Fig. 3. It is mainly extended in the same south-west direction as the X-ray/radio plerion. Unfortunately, there are no *Spitzer* images to combine a complete large scale picture of the extended mid-IR emission, around the Vela plerion including the TeV source. Nevertheless, a remarkable coin-

⁵ Obs. ID 1996, date 2002-01, exposure 49.5 ks, PI D. Helfand.

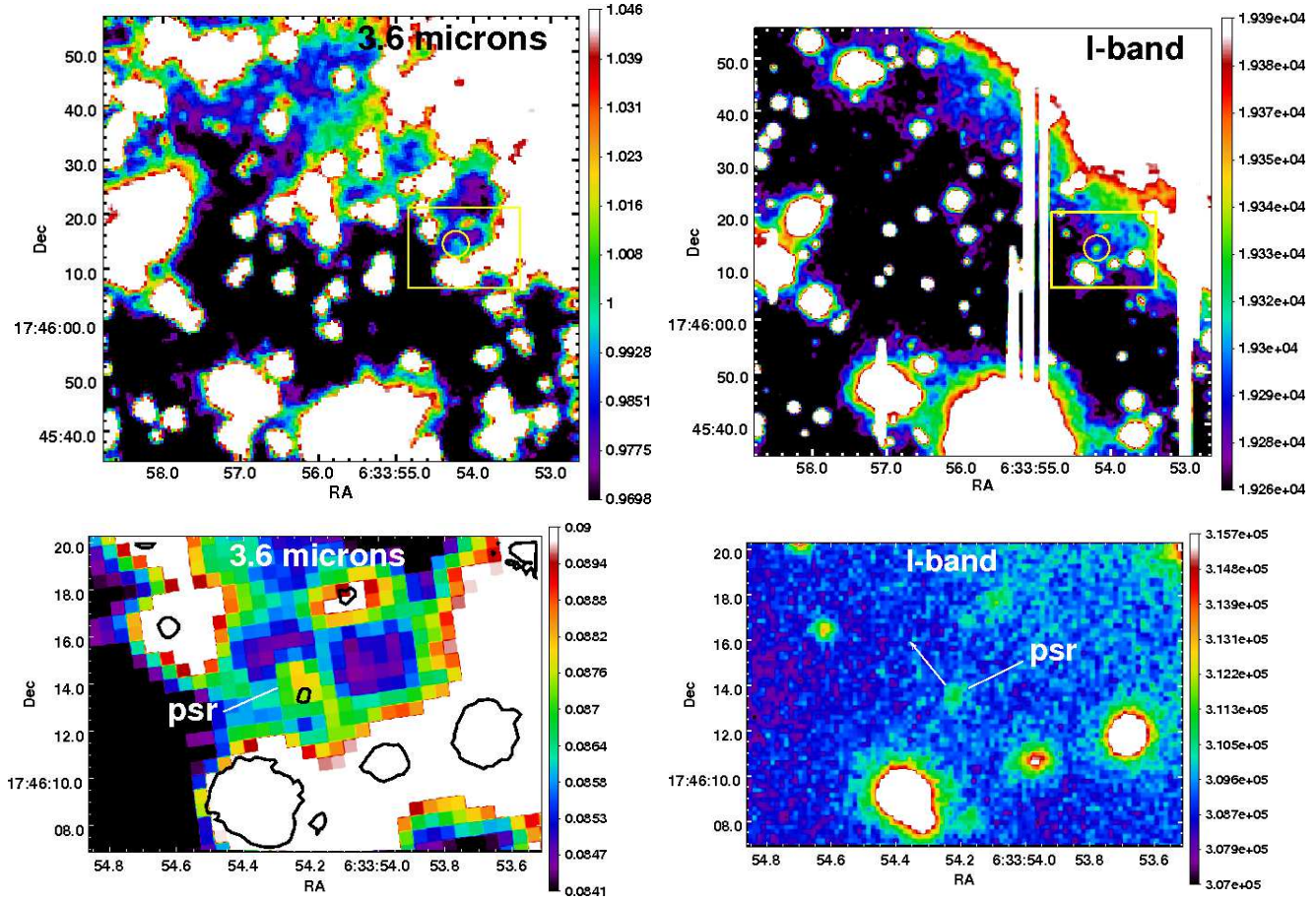


Figure 4. *Top panels:* An $\sim 1/2 \times 1/2$ overview of the Geminga field, as seen with the *Spitzer* (AORs 19037696+19037952) at $3.6 \mu\text{m}$ (left) and Subaru in the *I* band (right). The *I* band image is smoothed with four pixel Gaussian kernel, that is about the mid-IR pixel size. It is partially affected by several vertical stray light artefacts from oversaturated stars. Circles mark the Geminga optical counterpart and its mid-IR counterpart candidate. The $\sim 15'' \times 20''$ box region of the pulsar neighbourhood is enlarged in *Bottom panels*, where the Geminga counterpart is indicated by a line, and the arrow shows the direction of its proper motion. The contours in the bottom $3.6 \mu\text{m}$ image, where the only AOR 19037952 is implemented, are from the *I* band image.

cidence of its complicated east X-ray and radio boundary with the west boundary of the extended mid-IR emission suggests, that we likely see an interface between the pulsar wind and the SNR ejecta supported by a pressure balance between these two different fractions of the remnant. It is most clearly visible in the north-east part of the plerion, where a bright mid-IR protrusion fills a deep nebula bay between its north and south radio lobes. As seen from the radio image of Fig. 3, the magnetic field lines also lie along the protrusion/bay boundary, possible contributing to the pressure balance in this region. We see no extended mid-IR emission along the west plerion boundary. However, the magnetic field lines in the 5 GHz image are concentrated towards this boundary and mainly directed along it. The magnetic fields are stronger there and may play a key role in the shape and stability of the west part of the plerion.

3.2 Morphology of the Geminga field

3.2.1 Possible identification of the Geminga pulsar

In Fig. 4 we compare fragments of the Geminga field images obtained in the optical *I* band on January 2001 with

the Subaru telescope and at $3.6 \mu\text{m}$ with the *Spitzer*/IRAC. The *I* band image is taken from Shibano et al. (2006). The pulsar optical counterpart is indicated by the yellow circle in the top panels and by the thin line in the bottom ones, where an overview of the field and pulsar immediate vicinities are shown, respectively. The direction of the pulsar proper motion of $178.2 \pm 1.8 \text{ mas yr}^{-1}$ with a position angle of $52^\circ.9 \pm 0^\circ.4$ (Faherty et al. 2007) is shown by the arrow in the bottom *I* band image. For the $3.6 \mu\text{m}$ observation epoch the expected displacement of the pulsar from its *I* band position is $\approx 1''.22$. It is consistent at 1σ astrometric uncertainty level ($0''.4$) with the positions of a faint mid-IR source marginally detected at $3.6 \mu\text{m}$, that is also marked as 'psr'. The position of the source itself is defined with a twice worse accuracy of $\approx 0''.8$, as compared to the Vela counterpart candidate case. The main reason is its faintness and a poor approximation of the object brightness distribution by a point-like source profile. Nevertheless, it is fully compatible with the pulsar proper motion path, and can be considered as a likely mid-IR counterpart of Geminga.

Despite a worse spatial resolution of the *Spitzer* compared to the Subaru, as in case of the Vela pulsar, practically all background optical objects in the frames shown in Fig. 4

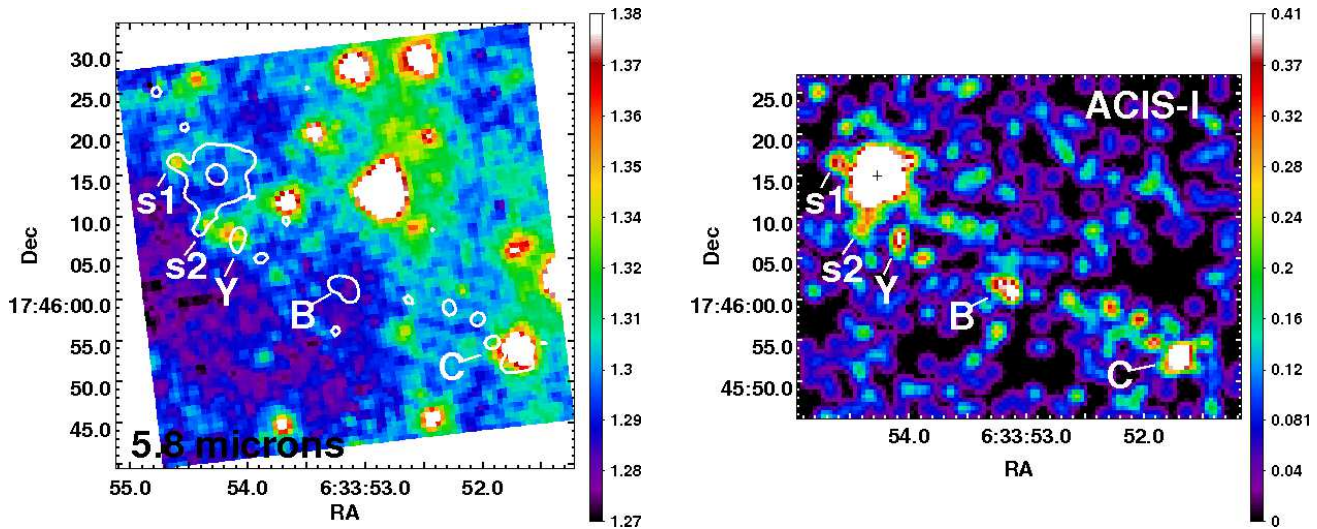


Figure 5. The large scale overview of the Geminga field at 5.8 μm (left) and in X-rays (right). The contours in mid-infrared image are from the X-ray image. Bright components of the clumpy Geminga tail, as well as the two background IR/optical sources, 's1' and 's2', are marked. Geminga, marked by the cross in the X-ray image, is not detected in this infrared band. A bright X-ray blob B and other less bright blobs have no infrared counterparts. While the blob C at the end of the X-ray tail is likely associated with a bright star, and the blob Y may be associated with a red background source not visible at shorter IR/optical wavelengths.

can be identified in the mid-IR and vice versa. This is underlined by black contours from the *I* band image, which are overlaid on the bottom mid-IR image. We have not found also any additional background object in immediate vicinity of Geminga in the near-IR image of the field obtained with the *HST* in the adjacent F160W band (Shibanov et al. 2006). Considering much larger FOV, as in the top panels of Fig. 4, we found only a few new faint mid-IR sources, which are not visible in the *I* band and located far away of the pulsar. Hence, the appearance of a new background source at the expected Geminga position in the mid-IR is very unlikely. This supports the correct identification of the pulsar.

Unfortunately, the suggested counterpart candidate, is detected only at $\sim 2\sigma$ level and only in the one *Spitzer* band. Combining the data from the two AORs (19037696+19037952), as is in the top panel of Fig. 4, has not allowed us to increase the significance of its detection due to a high Zodiacal background in the first AOR, though the source is seen at the same coordinates in both AORs (see Sect. 2.1). Therefore, this source has to be considered with a caution and needs a confirmation by deeper observations. Nevertheless, summarizing all pros and contras, we will assume below, that the source is the real counterpart of Geminga, and estimate how this may affect the broadband spectrum of the pulsar.

3.2.2 Searching for the Geminga PWN

Deep X-ray observations have allowed to find fragments of a bow shock and an axial tail of Geminga at the distances of several arcminutes behind the pulsar (Caraveo et al. 2003; Pavlov et al. 2010). We have not found any significant mid-IR counterpart of the bow shock at these scales. At the same time, the tail was found to consist of a time-variable clumps appearing and disappearing in various places from time to time (Pavlov et al. 2010), and a few possible counterparts of the clumps can be considered. An overview of the pulsar

field containing the whole extent of the axial tail is shown in Fig. 5, where we compare the mid-IR 5.8 μm and ACIS-I⁶ X-ray images. To go as deep as possible, the mid-IR image was combined from the two longest observations listed in Table 1 (AORs 19037696 and 19037952). The brightest fragments of the X-ray tail detected at the ACIS-I observation epoch are marked by B and C, in Pavlov et al. (2010) notations, and yet another one by Y. The X-ray contours are overlaid on the mid-IR image.

There is no any significant mid-IR counterpart for the X-ray time-variable B substructure. It was not seen in the early ACIS-S⁷ X-ray image and, hence, has been born at a time within a 3.5 yr interval between the two X-ray observations. If we assume that appearing a bright X-ray clamp is accompanied with an optical/IR emission, then the absence of B in the mid-IR suggests, that it was created either after the *Spitzer* observations and its age is $\lesssim 9$ months, or it has flashed before these observations, but the lifetime of the particles responsible for possible mid-IR afterglow associated with the X-ray flash is much shorter than that for the particles radiating in X-rays.

The blob C nicely coincides with a background stellar source, as has been noticed by Pavlov et al. (2010). We can add, that in the mid-IR this source is not a single but likely a blend of one bright an 2–3 fainter stars.

The blob Y positionally coincides with a faint background source in the 5.8 μm image. The source is not visible at shorter wavelengths and hardly visible at 8 μm . This blob is close to a bright blob A, that was clearly visible in the early ACIS-S image (see, Pavlov et al. 2010) and not seen in the ACIS-I image shown here, as well as in any available IR/optical image. It is not clear, whether this is a remnant of A, that has faded and moved by $\sim 3''$ to the east from its initial X-ray position, or it is an independent substructure,

⁶ Obs. ID 7592, date 2007-08, exposure 72.1 ks, PI G. Pavlov.

⁷ Obs. ID 4674, date 2004-02, exposure 18.8 ks, PI D. Sanwal.

Table 2. The results of the aperture photometry for the presumed mid-IR counterparts of the Vela and Geminga pulsars. The 3rd column shows the magnitudes and upper limits measured using optimal aperture radii presented in the 2nd column. The presented aperture correction factors are for the flux.

| λ_{eff} | apert. radi- us | mag. measur- ed ^a | apert. correc- tion factor | mag. correc- ted ^a | log F |
|-------------------|-----------------------|------------------------------------|-------------------------------------|-------------------------------------|--------------------|
| (μm) | (pix) | (mag) | | (mag) | (μJy) |
| Vela | | | | | |
| 160 | 8 | $\gtrsim 2.34$ | 1.9 | $\gtrsim 1.64$ | $\lesssim 4.5$ |
| 70 | 8.7 | $\gtrsim 6.3$ | 1.2 | $\gtrsim 6.1$ | $\lesssim 3.44$ |
| 24 | 5.3 | $\gtrsim 11.41$ | 1.16 | $\gtrsim 11.25$ | $\lesssim 2.35$ |
| 8.0 | 10 | $\gtrsim 15.65$ | 1.07 | $\gtrsim 15.58$ | $\lesssim 1.70$ |
| 5.8 | 4 | 16.73(27) | 1.38 | 16.38(27) | 1.51(11) |
| 4.5 | 10 | $\gtrsim 16.90$ | 1.06 | $\gtrsim 16.84$ | $\lesssim 1.52$ |
| 3.6 | 4 | 18.69(22) | 1.21 | 18.48(22) | 1.06(09) |
| Geminga | | | | | |
| 24 | 5.3 | $\gtrsim 11.25$ | 1.16 | $\gtrsim 11.09$ | $\lesssim 2.42$ |
| 8.0 | 10 | $\gtrsim 16.3$ | 1.07 | $\gtrsim 16.23$ | $\lesssim 1.44$ |
| 5.8 | 10 | $\gtrsim 18.9$ | 1.06 | $\gtrsim 18.84$ | $\lesssim 0.52$ |
| 4.5 | 10 | $\gtrsim 20.48$ | 1.06 | $\gtrsim 20.42$ | $\lesssim 0.09$ |
| 3.6 | 4 | 21.77(78) | 1.21 | 21.56(78) | -0.18(31) |

^a numbers in brackets are 1σ uncertainties referring to last significant digits quoted

that was flashed later in the time interval between the two X-ray observations. Additional X-ray and mid-IR observations are necessary to understand whether the Y blob and the suggested IR counterpart are variable and have the same origin or not. If we indeed detected this blob almost simultaneously in the X-ray and mid-IR, it could be younger than the blob B. The rest fainter and less extended X-ray sources possible related to the extended tail are not identified in the mid-IR.

Considering immediate vicinity of the pulsar, Pavlov et al. (2010) discussed a bow shock structure of the X-ray PWN with possible ‘forward-jet’, which is directed north-east of Geminga along its proper motion. As seen from Fig. 5, the forward-jet substructure, marked as ‘s1’, is likely not related to the PWN, but is the X-ray counterpart of a red star-like background optical object, that is also detected in the near-IR and optical images (cf. Fig. 4). In the deep ACIS-I image its profile overlaps with the outermost region of the nebula producing a false impression on the presence of a jet. The object s1 is also visible as a point-like isolated object in the ACIS-S image, where the exposure was short. A similar situation is for an apparent south-east ‘protrusion’ seen only in the ACIS-I image and marked as ‘s2’. It is likely to be a background source as well, that is brighter in the optical/IR, but fainter in X-rays as compared to ‘s1’.

3.3 Photometry of counterpart candidates

To minimize the flux contamination of the detected pulsar counterpart candidates from nearby background objects the

aperture photometry was performed on the star-subtracted IRAC images.

For magnitude estimates we used IRAF *daophot* tasks with zero points given in the IRAC Instrument Handbook⁸. Prior photometric measurements, we converted each image from MJy steradian⁻¹ to DN units using the conversion factors from image fits headers. In this case the *daophot* magnitude error output can be directly used for the flux uncertainty estimates. To find an optimal aperture radius based on the maximal signal to noise ratio, photometric growth curves were obtained and used. For the pulsar candidates at 3.6 and 5.8 μm the optimal circular aperture radius was 4 pixels (at 0.6 pixel scale) with the background annulus and dannulus in the ranges of 5–6 and 4–6 pixels, respectively. The measured fluxes were multiplied by aperture correction factors taken from the IRAC Data Handbook⁹. We have performed the PSF photometry as well and got the results consistent with the aperture photometry at 1σ level.

Conservative 3σ point source magnitude upper limits can be placed for the counterpart candidates in the mid-IR bands where the pulsar fields have been observed but no candidates were found. To do that, the circular aperture radii were selected encapsulating $\gtrsim 80\%$ of a potential point source flux, the apertures were centred at the pulsar positions, and standard deviations and inherent flux variations within these apertures were used. The magnitudes were converted into fluxes in physical units and the results are summarized in Table 2. For Geminga at 3.6 μm , where the counterpart candidate is visible only at 2σ level, the data from the AORs 19037952 and 19037696 (Table 1) provide consistent results. However, the flux uncertainty is smaller for the former AOR, where the Zodiacal background is lower, and we use this result for our further analysis.

3.4 Multiwavelength spectra

Let us assume that our mid-IR identifications are real, and consider, how this can affect the spectra of the pulsars. Using the measured mid-IR fluxes, available optical and UV data, in Fig. 6 we compile dereddened multiwavelength spectra of the Vela and Geminga pulsars in the mid-IR-UV range, and compare them with the respective spectrum of the Crab pulsar taken from Sandberg & Sollerman (2009). The interstellar extinctions $E(B-V)$ are 0.055 and 0.023 mag towards Vela and Geminga, respectively (Shibanov et al. 2003, 2006). These are small enough, and dereddening corrections in the mid-IR bands are negligible as compared to the measured flux uncertainties. For instance, the magnitude correction $\Delta\lambda$ at $\lambda = 3.6 \mu\text{m}$ is $\lesssim 0.01$ mag for both objects. For clearness, in Fig. 6 we notify the broad bands, where pulsar fluxes were measured, and indicate which ones were obtained with the *Spitzer*/IRAC or with the MIPS.

In contrast to the Crab, that shows almost a flat spectrum in the considered range, the compiled spectrum of the Vela pulsar demonstrates a strong, an order of magnitude, mid-IR flux excess, that progressively increases with the wavelength, as compared to the optical range. Geminga

⁸ see, <http://ssc.spitzer.caltech.edu/irac/iracinstrumenthandbook/>

⁹ IRAC Data Handbook, table 5.7.

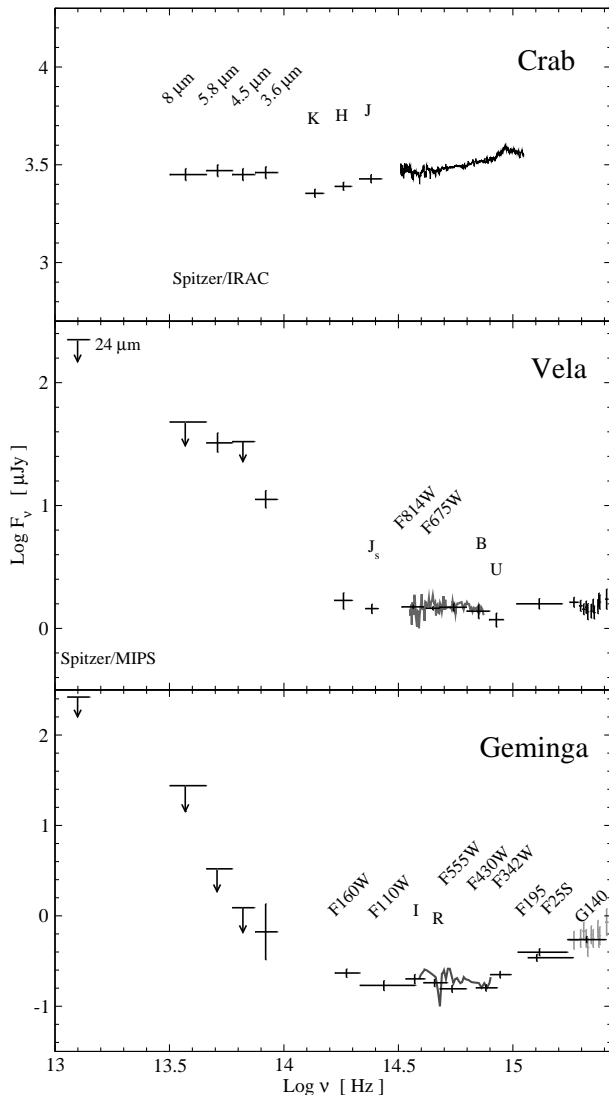


Figure 6. Unabsorbed spectra of the Crab, Vela, and Geminga pulsars from the mid-IR to the optical-UV. The Crab data are from Sandberg & Sollerman (2009). The Vela UV, optical, and near-IR data are from Romani et al. (2005), Mignani et al. (2007), and Shibano et al. (2003), respectively. The Geminga UV and optical/near-IR data are from Kargaltsev et al. (2005) and Shibano et al. (2006), respectively, the optical spectrum is from Martin, Halpern & Schiminovich (1998).

shows a similar, though much less significant, excess, as follows from its marginal detection. It is important to note, that an intention of the flux increase towards the IR has been noticed by Shibano et al. (2003, 2006), when both pulsars were identified in the near-IR *JH* bands. However, the significance of that was low, and the presence of such a strong mid-IR excess was difficult to expect, based on the flat spectrum of the Crab pulsar, that has been so far the only rotation-powered pulsar detected in the mid-IR. The mid-IR fluxes of the Vela and Geminga candidates are likely to be in agreement with their near-IR counterpart fluxes, confirming the reality of the apparent flux increases towards the IR, resulted early only from the near-IR data. Thus, the compiled spectra appear to be real, but not the tenta-

tive ones. We consider this as an additional evidence, that the detected mid-IR emission is indeed associated with the pulsars.

Accepting that, we can now update the rotational phase averaged spectral pictures for both pulsars in the whole observational range, from the radio to hard γ -rays (cf. Shibano et al. 2003, 2006), including our mid-IR data, and the data obtained recently with the *Fermi* γ -ray observatory (Abdo et al. 2010a,b).

As seen from Fig. 7, the flux density of the mid-IR emission from the Vela pulsar becomes comparable with the density of the spectral bump produced by thermal emission from the atmosphere (atm.) at the surface of the NS visible in soft X-rays. At the same time, within large uncertainties it may be compatible with the long wavelength extrapolation of the nonthermal soft X-ray spectral tail detected with *Chandra* and the *RXTE* and described by a power-law (hatched region). The mid-IR flux upper limits are still lower than flux densities of a coherent radiation at radio frequencies.

Similar spectral behaviour is observed for Geminga. The main difference is that Geminga is fainter in the optical/IR, and the observed mid-IR excess is much less significant. Nevertheless, the steep IR flux increase towards low frequencies can not be excluded by the derived mid-IR flux upper limits. This suggests, that at several 10s microns the mid-IR flux density might be comparable with the soft X-ray thermal blackbody-like emission bump from the Geminga surface (BB) and compatible with the low frequency extension of the nonthermal soft-X-ray spectral tail, as in the Vela case.

However, from the spectral behaviour of both pulsars shown in Fig. 6 and Fig. 7, it is most likely that the *Spitzer* mid-IR observations reveal us a new spectral component in the emission of these rotation powered-pulsars, whose origin is different from those of the rest components detected early, and, perhaps, from that of the Crab in the mid-IR.

4 DISCUSSION

Subarcsecond positional coincidence of the detected point-like object at 3.6 and 5.8 μ m with the Vela pulsar coordinates suggests, that this object is likely to be the mid-IR counterpart of the pulsar. This is also supported by the consideration of its spectral energy distribution (SED), showing that the measured mid-IR fluxes are compatible with the long wavelength spectral excess observed early in the near-IR. The same is likely to be true for fainter Geminga, with a caution that its mid-IR counterpart candidate is detected only marginally and solely in the 3.6 μ m band. Additional confirmations can be obtained from near-IR detections of both pulsars in the *K* band, where they have not been observed, and by deeper mid-IR observations, to detect the Geminga counterpart with a higher significance and to establish both identifications by proper motion measurements of the counterparts in this range and checking their consistency with the proper motions of the pulsars. Extension of the pulsar observations to the far-IR would be also useful in this context.

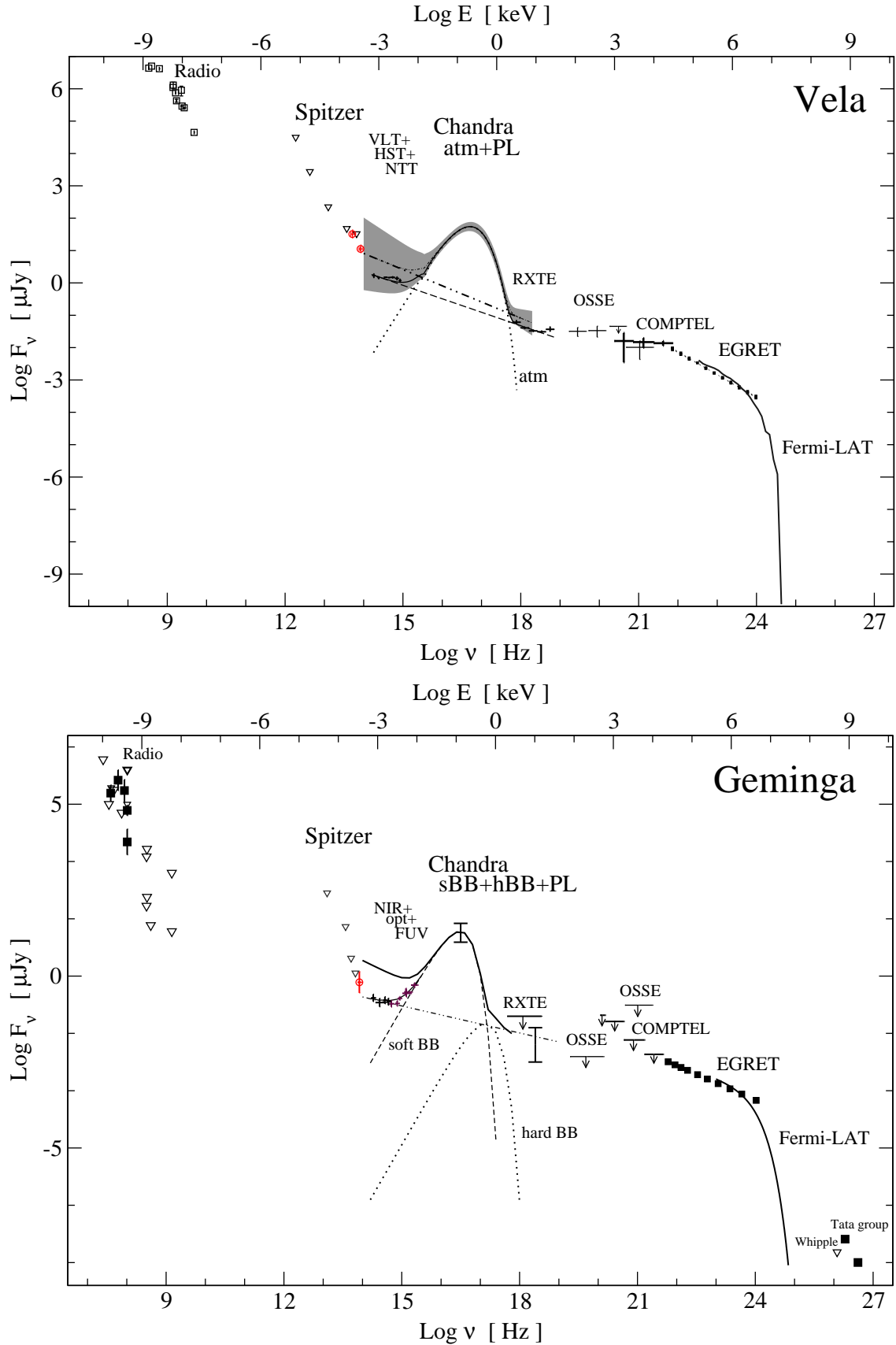


Figure 7. Multiwavelength unabsorbed spectra for the Vela and Geminga pulsars from the radio to hard γ -rays compiled from the data obtained with different instruments, as indicated in the plots. Mid-IR fluxes are marked by red circles. Down triangles mark upper limits. Filled squares in the radio range of Geminga are its radio detections by Malofeev & Malov (1997).

4.1 The nature of the mid-IR excess

If our mid-IR identifications of the two pulsars are real, the question is what is the nature of the observed mid-IR flux excesses.

Besides the Crab, where the excess is likely to be marginal (Sandberg & Sollerman 2009), there are only two other isolated NSs detected in the mid-IR. These are the AXPs 4U 0142+61 (Wang et al. 2006) and 1E 2259+586 (Kaplan et al. 2009). Both have been widely considered as radio-silent¹⁰, and belong to a class of magnetars, i.e., NSs with extremely strong magnetic fields. They have significant mid-IR excesses, which have been interpreted as the emission from X-ray irradiated fall-back discs around the NSs. Such discs can be formed around isolated NSs through a process of supernova fall-back (Chevalier 1989).

The marginal excess over the power-law extrapolation of the optical SED for the Crab was suggested to be caused by a nearby PWN knot located in 0.6 from the pulsar. The knot is much fainter than the pulsar in the optical, but it has a very red spectrum with a steep flux increase towards the mid-IR, where the knot brightness can be comparable to that of the pulsar (Sandberg & Sollerman 2009). This can result in an overestimation of the measured pulsar flux in this range, since the *Spitzer* spatial resolution does not allow one to resolve the knot from the pulsar.

A planet, or a cool low-mass stellar companion could also provide an excess. However, this is unlikely for our pulsars, since no planets or binary companions have been reported from timing observations of Vela and Geminga¹¹.

Finally, the observed excesses can be produced in magnetospheres of the pulsars. The latter possibility has also not been excluded for the magnetar 1E 2259+586 (Kaplan et al. 2009). Below we discuss in more detail the possibilities listed above for the interpretation of the Vela and Geminga SEDs. We will focus mainly on the Vela pulsar, whose mid-IR counterpart candidate is firmly detected.

4.1.1 The fall-back disc

As protoplanetary discs around ordinary pre-main sequence stars (e.g., Dullemond & Monnier 2010) or dust discs detected around white dwarfs (e.g., Melis et al. 2010; Farihi 2010), the fall-back discs around pulsars can lead to emission excesses in pulsar spectra in the mid-IR and submillimetre bands (Foster & Fischer 1996; Perna, Hernquist & Narayan 2000).

To find out whether the Vela and Geminga spectral excesses can be explained by radiation from hypothetical discs around these objects, following Wang et al. (2006), we consider passive dust discs heated by X-ray irradiation from the pulsars. We adopt a model of the irradiated disc emission from Vrtilek et al. (1990). It is assumed that there is enough gas to provide the pressure support for the dust, but its contributions to the heating balance due to a viscous dissipation and the emission are negligible. In this model the

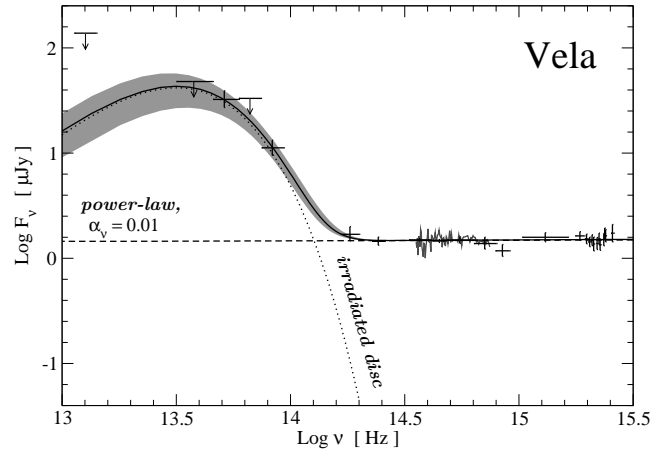


Figure 8. The spectral fit of the dereddened Vela pulsar optical-IR SED by a sum of the fixed power-law component (dashed line), which describe contribution from the pulsar itself, and X-ray irradiated passive dust disc model (dotted line). The solid line is the best-fitting result and the hatched region shows 1σ uncertainty of the fit. The dotted line is the contribution from the thermally emitting disc with the best-fitting parameters. For the parameters see the text.

disc is optically thick and at a fixed disc radius it radiates as blackbody with a temperature depending on the radius $\propto R^{-3/7}$ (Vrtilek et al. 1990). The parameters determining the emission properties of the disc are the inclination angle ζ , albedo η , and the internal and external disc radii R_{in} and R_{ex} . All of them cannot be certainly constrained from the spectral fit to the observed IR SEDs containing only four points and upper limits. One has to select most critical ones to be found from the fit, and fix the others at reasonable values. Albedo strongly affect the results and in our fits we fixed it using a set of values between 0.5 and 1. We fixed also possible contributions from the pulsars in the IR, assuming that in this range their spectra are consistent with a power-law extrapolation from the optical-UV range. The observable disc properties depend also on the X-ray luminosity of the pulsar and its distance, which are known for our pulsars from previous studies: $L_X^{Vela} = (5.3 \pm 0.5) \times 10^{32}$ erg s⁻¹ (Pavlov et al. 2001), $L_X^{Gem} = (3 \pm 1) \times 10^{31}$ erg s⁻¹ (Kargaltsev et al. 2005), $d^{Vela} = 287_{-17}^{+19}$ pc (Dodson et al. 2003), and $d^{Gem} = 250_{-60}^{+120}$ pc (Faherty et al. 2007).

For Vela the inclination angle can be fixed at 64° , accounting for the viewing angle of the pulsar rotation axis, estimated based on the PWN geometry (Helfand et al. 2001; Ng & Romani 2008). Within uncertainties this angle is compatible with that derived from the polarimetric radio observations of the pulsar (Johnston et al. 2005). We assume, that the disc and pulsar rotation axes coincide with each other. As a result, the irradiated disc model provides a good fit for the Vela SED at $\eta < 0.85$. An example is presented in Fig. 8 where we fixed η at 0.75. In this case $R_{in} = 0.28 \pm 0.05 R_\odot$, $R_{ex} = 1.4 \pm 0.4 R_\odot$, and the dust temperatures at the inner and external disc boundaries $T_{in} = 834 \pm 63$ K, and $T_{ex} = 418 \pm 56$ K, respectively.

The R_{in} value derived from the fit is much larger than the pulsar light cylinder radius $R_{LC} \approx 0.6 \times 10^{-2} R_\odot$. This allows Vela to work as the radio pulsar. At the same time

¹⁰ See, however, Malofeev et al. (2005); Malofeev, Teplykh & Malov (2010).

¹¹ Possible planet orbiting Geminga (Mattox, Halpern & Caraveo 1998) hasn't been confirmed by recent analysis.

it is about ten times smaller than that of AXP 4U 0142+61 (Wang et al. 2006), suggesting a more compact disc around the Vela pulsar than the disc around the AXP, while the inner disc temperatures for both NSs are similar and consistent with the sublimation temperature of dust $\gtrsim 1000$ K. This is not a surprise, since the X-ray luminosity of the AXP, 9×10^{35} erg s $^{-1}$, is about three orders of magnitude higher than that of the Vela pulsar, and the AXP dust disc can survive only at larger distances from the NS. Therefore, R_{in} derived from the fit is in agreement with the inner disc boundary, that can be estimated independently from the dust destruction temperature, as it has also been noticed by Wang et al. (2006) for the 4U 0142+61 case. We also note, that our R_{ex} value is compatible with a condition $R_{ex} \lesssim R_{\odot}$ found to be correct for almost all dust discs observed around white dwarfs (Farihi 2010). This means that R_{ex} cannot exceed the Roche radius, within which any rocky object would be tidally disrupted (Melis et al. 2010). The Roche radius for NSs, as for white dwarfs, is about R_{\odot}^{12} .

If $R_{in} \gg R_{LC}$, then fall-back discs around isolated pulsars can be swept away by radiation pressure of the intensive magneto-dipole radiation of the pulsar (Shvartsman 1970). However, it was shown (Ekşi & Alpar 2005), that such a disc is not disrupted by this process, if $R_{in} \lesssim 2R_{LC}$ and $R_{in} \lesssim 100R_{LC}$ in cases of the orthogonal and aligned magnetic rotators, respectively. For Vela our best fit value $R_{in} \approx 45R_{LC}$ lies in the middle of this range, providing stability of the disc against the radiation pressure at the angles between the magnetic and rotational axes of the pulsar $\lesssim 10^\circ$. This is in contrast to a value of $\sim 70^\circ$ estimated from a combination of the pulsar polarimetric observations (Johnston et al. 2005), and X-ray PWN geometry analysis (Ng & Romani 2008). The latter value suggests the disruption of the disc, since at this angle we cannot obtain any reasonable fit to the Vela SED with R_{in} , that is close enough to the R_{LC} value to satisfy the stability criterion. Nevertheless, if the Vela pulsar is indeed closer to the orthogonal rotator, but not to the aligned one, the disc might still survive, if we assume that optically thin gas disc component exists inside R_{in} , as it is for dust discs around pre-main-sequence stars (Dullemond & Monnier 2010). This component cannot contribute significantly to the IR emission, but may support the stability of the disc against the radiation pressure.

At the same time, the problem of the dust disc structure and stability in the presence of a strong relativistic particle wind from energetic pulsars is still not resolved (see, e.g., Bryden et al. 2006; Jones 2007, and references therein). The presence of the planetary system orbiting PSR B1257+12 (Wolszczan 1994) strongly suggests that its formation must involve a preplanetary disc circling the NS. Despite of many efforts (Bryden et al. 2006), the most stringed upper limits on the dust disc emission in this system obtained with the *Spitzer*/MIPS, suggests that the dust, if it really exists there, is significantly cooler than that derived by us for the Vela pulsar and by Wang et al. (2006) for AXP 4U 0142+61. Therefore, we conclude, that a simplified model of a passive dust disc can formally explain the IR excess for Vela, but

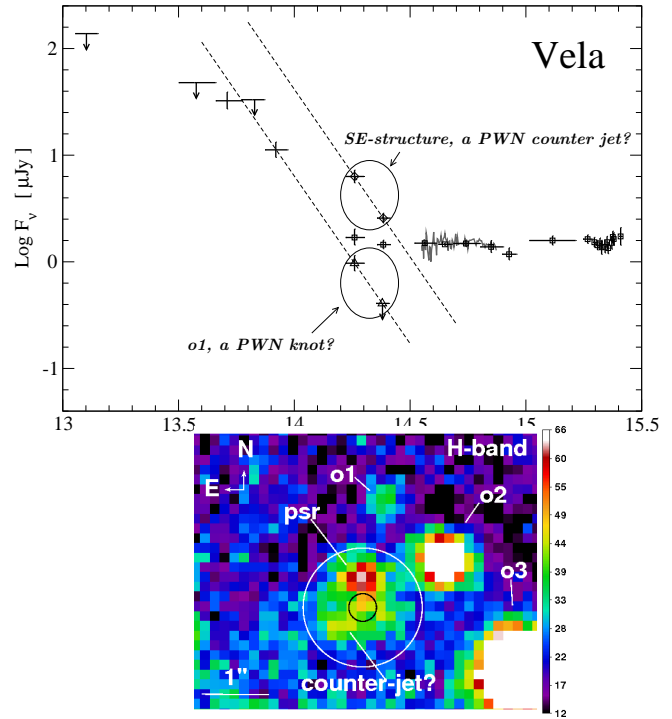


Figure 9. The comparison of the spectral energy distributions for the likely Vela pulsar counterpart and the two structures located in $\sim 2''$ vicinity of the pulsar and projected on the NW X-ray PWN jet ('o1') and the SE counter-jet of the PWN (SE-structure), shown in the attached fragment of the *H* band image. The data-points of the structures are outlined by ellipses and notified in the top panel plot, while the rest points belong to the pulsar counterpart. Dashed lines show tentative spectral fits for these structures by power laws with similar spectral indices of about 3.1. As seen, the spectral slope of the pulsar counterpart candidate in the IR is compatible with the spectral slopes of the structures. Large and small circles in the image indicate the FWHM of the PSF and the pulsar position with its 1σ uncertainty in the mid-IR, respectively

it is not clear, whether such a disc can survive around this energetic pulsar.

We note also, that the Vela IR SED can be roughly fitted by a pure blackbody model with $T \approx 597$ K, and a blackbody radius of $\approx 0.7 R_{\odot}$. The latter one is too large for a planet or a cool brown dwarf. This is an additional argument against a cool binary companion of the pulsar as a source of the excess.

We have carried out the similar analysis for Geminga. The results are very uncertain due to larger uncertainties of its IR fluxes. We can note only that the fall-back disc around Geminga cannot be excluded by current data. The inner disc radius seems to be comparable with the Geminga light cylinder radius, $R_{LC} \approx 0.016 R_{\odot}$, perhaps, suggesting the disc stability, that may lead to unstable behaviour of Geminga as the radio pulsar (Malofeev & Malov 1997). However, deeper IR studies are necessary to make any definite conclusions.

¹² The exact value depend on the density of a rocky object as well as on mass and radius of a star (Melis et al. 2010).

4.1.2 An unresolved PWN structure

As in the Crab case, the IR excesses of Vela and Geminga may be produced by unresolved nearby structures of their PWNe.

There are two faint red structures in $\sim 2''$ vicinity of the Vela pulsar, which have been detected in the near-IR (Shibanov et al. 2003). They are projected on the X-ray PWN jet and counter-jet, and can be barely resolved in the bottom-left panel of Fig. 1. For clearness the respective region is enlarged in the bottom panel of Fig. 9. A knot-like object 'o1' is located $\approx 1.2''$ NW of the pulsar and detected in the H band. An extended $\approx 1.5''$ structure is located just SE of the pulsar, partially overlapping with it, and detected in the J and H bands. Both objects are not seen in the optical bands, and the SE structure has showed some signs of a short-time variability in the near-IR (Shibanov et al. 2003). The SED of 'o1' with $F_J \lesssim 0.4 \mu\text{Jy}$ and $F_H = 0.97(18) \mu\text{Jy}$ can be extrapolated to the mid-IR using a power-law with a spectral index¹³ $\alpha_\nu \approx 3$ (Fig. 9). This fact, and the spatial separation of 'o1' from the pulsar, that is comparable to that of a nearby west star ('o3', in Shibanov et al. (2003) notations) visible in the mid-IR and optical (cf. Fig. 1), suggest that it could be detected in the *Spitzer*/IRAC bands at a similar brightness level as the pulsar candidate in the wing of its PSF, whose mid-IR position and FWHM are marked by circles in the bottom panel of Fig. 9. However, we do not detect it there. This means, that either 'o1' has a very peculiar and unrealistic SED with a sharp flux peak in the H band, or it is a time variable object. If 'o1' and the SE structure are associated with the Vela PWN, the latter assumption is compatible with a strong time variability of the PWN observed in X-rays (Pavlov et al. 2001a). As seen from Fig. 9, at the epoch of the near-IR observations the integral brightness of the SE structure, with $F_J = 2.59(12) \mu\text{Jy}$ and $F_H = 4.94(38) \mu\text{Jy}$, was higher than the brightness of the pulsar, while 'o1' was fainter. The spectral slopes of both structures are comparable to each other and to the spectral slope of the pulsar candidate in the mid-IR. Since the SE structure cannot be resolved from the pulsar in the *Spitzer* images, it can considerably contaminate the measured pulsar fluxes, assuming that the emission intensity of this structure in the mid-IR is compatible with the long wavelength extrapolation of its near-IR SED. This may be also supported by our astrometry, that shows a marginal shift of the mid-IR candidate position (black circle in the image of Fig. 9) from the near-IR counterpart centroid toward the SE structure.

We can then speculate, that the SE structure can, at least partially, explain the observed excess, if this structure became fainter at the *Spitzer* observation epoch, as it is for 'o1', but saved its steep spectral slope. In this case, we can expect a variation of the excess intensity with time, if the SE structure is indeed associated with the PWN, that varies with time. New *Spitzer*/IRAC observations in 3.6 and 5.8 μm , and high spatial resolution observations in the near-IR K_S band would be useful to verify that. We note, that the spectra of 'o1' and the SE structure are apparently about 2–3 times steeper than the spectrum of the Crab knot with $\alpha_\nu \approx 1.3$ (Sandberg & Sollerman 2009) and the X-ray spectrum

of the PWN. The reasons for that are not clear (see, e.g., Shibanov et al. 2003), and further IR observations can help to understand their real nature.

The object 'o2' is also not visible in the mid-IR, while it is detected in the optical RI and near-IR JH bands, showing that it is likely to be a distant ($\lesssim 10$ kpc) main sequence background star (Shibanov et al. 2003). For instance, for M0V star with the observed colour $J-H \approx 1$ at a Galactic $A_V \approx 4$, we obtain $d \approx 10$ kpc and the expected fluxes at 3.6 and 5.8 μm of $\lesssim 1.5\text{--}2.5 \mu\text{Jy}$. This is below the *Spitzer* observation detection limits and about 20 times fainter than the candidate flux at 5.8 μm . Therefore, the much brighter candidate can not be significantly contaminated by 'o2', even if its PSF overlaps with this star.

4.1.3 Pulsar magnetospheric emission

As seen from Fig. 7, the nonthermal magnetospheric emission dominates multiwavelength spectra of both pulsars from the radio to γ -rays, except of a narrow range in soft X-rays, where the thermal radiation from the surfaces of the NSs is more intensive. The spectra are mainly of a power-law, but their slopes are different in different spectral domains, and there are several spectral breaks, e.g., between the γ -rays and the hard X-rays, the soft X-rays and the optical, etc. These features are not yet clearly understood, and in this context, a new break between the optical and IR does not look very exclusive, and may represent an additional component of the NS magnetospheric emission.

Except of the Crab, three, of four young PWNe so far identified in the optical-IR (PSR B0540–69, 3C 58, and G292.0+1.8, (Williams et al. 2008; Serafimovich et al. 2004; Shibanov et al. 2008; Slane et al. 2008; Zharikov et al. 2008; Zyuzin et al. 2009) show strong mid-IR excesses with steep power-law spectral slopes in the IR. It might be possible, that the relativistic particles responsible for these IR excesses are ejected from magnetospheres of the pulsars powering the PWNe. In this case, the same particles can provide the IR excesses in the magnetospheric emission of the pulsars.

However, only the detection of pulsations with pulsar periods would be a strong evidence on the NS magnetospheric origin of an enhanced emission observed for Vela and tentatively for Geminga in the IR. Until the time, when timing observations of pulsars in the IR will be possible, imaging observation of other suitable rotation powered pulsars in the IR would be useful, to expand the sample of NSs detected in this range and to verify, if the IR excess, like that of Vela and Geminga, is a more common feature in the pulsar emission, than a flat optical-IR SED of the Crab.

4.2 Mid-IR PWN signatures

The inner torus-like PWNe structures around the young Crab, J1124–5916, J0205+6449, and B0540–69 pulsars are well identified in the optical and mid-IR (Sandberg & Sollerman 2009; Zharikov et al. 2008; Zyuzin et al. 2009; Shibanov et al. 2008; Serafimovich et al. 2004; Williams et al. 2008). The latter three objects are even brighter in the IR than in the optical, and their SEDs demonstrate a steep flux increase toward longer wave-

¹³ The index α_ν is defined as $F_\nu \propto \nu^{-\alpha_\nu}$.

lengths. In all cases the optical/IR PWN counterparts have approximately the same sizes as in X-rays.

The Vela and Geminga pulsars are considerably older and less energetic, as compared to the above group, and their X-ray PWNe are fainter as well. This is likely to be the main reason why we do not observe PWNe counterparts of these pulsars in the optical and IR at the same spatial scales as they are seen in X-rays. However, we cannot exclude the presence of a hint of a counter-jet fragment at a small distance from the Vela pulsar. As have been discussed above, such poorly resolved small scale structures can be a reason of the observed IR excesses in the pulsar SEDs. The compactness of these structures, if they are real, show that the inner PWN evolves with the pulsar age and fade more rapidly at longer wavelengths than in X-rays. We note also, that there are still no reports on the detection of the inner tours-like structure with jets for the Vela PWN in the radio range, while a 10 arcsec long Geminga tail structure was recently detected with the VLA at 4.5 GHz (Pellizzoni et al. 2011). The Geminga radio flux density is compatible with the long wavelengths extension of the tentative mid-IR excess reported here.

At the same time, the mid-IR observations allowed us to define more exactly the Geminga X-ray PWN shape in the immediate vicinity of the pulsar. Its forward-jet and the south-east protrusion are likely not to be the real PWN structures, but are X-ray counterparts of background red stellar object 's1' and 's2' (Fig. 5). The same is true for the distant blob C, that coincides with a bright IR background object. More careful X-ray spectral analysis is necessary to confirm or reject the nature of the 's1' and 's2' objects, that is outside the scope of this paper.

The comparison of the X-ray and 8 μ m images of Vela shows a good coincidence of the west boundary of the extended IR emission of the remnant with the east boundary of the large scale X-ray plerion (Fig. 3). Further comparison of the mid-IR image with the high spatial resolution radio images of the Vela plerion, obtained with the ATCA by Dodson et al. (2003a), likely supports this statement. A bay between the north and south plerion lobes in the radio image is filled by a bright protrusion of the extended mid-IR emission. The magnetic field lines lie along the bay/protrusion boundary, also suggesting that we likely see an interface between the relativistic pulsar wind and a dust SNR ejecta provided by the pressure balance between these two different parts of the remnant. No lobes structures are visible in the optical (cf., Mignani et al. 2003) and more careful analysis is necessary to check this hypothesis.

To summarize, we conclude, that *Spitzer* mid-IR observations have opened a new spectral window for the study of the pulsars. The detections of the likely counterparts of the Vela and Geminga pulsars, and PWNe for several Crab-like pulsars reveal strong mid-IR excesses in the emission of these objects, that was rather difficult to expect in advance. Further mid-IR studies of these and other pulsars are necessary to increase the number of the objects detected in the IR, and understand the nature of their emission in this range.

ACKNOWLEDGMENTS

This work is based on observations made with the *Spitzer* Space Telescope, which is operated by the Jet Propulsion Laboratory, California Institute of Technology under a contract with NASA. We are grateful to anonymous referee for useful comments improving the paper. AAD, DAZ and YAS acknowledge support from the Russian Foundation for Basic Research (grants 08-02-00837 and 09-02-12080), Rosnauka (Grant NSh 3769.2010.2), and the Ministry of Education and Science of the Russian Federation (Contract No. 11.G34.31.0001). SVZ acknowledges support from CONACYT 48493 and PAPIIT IN101506 projects. DAZ acknowledges support from St. Petersburg Government grant for young scientists (2.3/04-05/008).

REFERENCES

- Abdo A. A. et al., 2008, *Phys.Rev.Lett.*, 101, 221101
- Abdo A. A. et al., 2010a, *ApJ*, 713, 154
- Abdo A. A. et al., 2010b, *ApJ*, 720, 272
- Abdo A. A. et al., 2010c, *ApJ*, 713, 146
- Aharonian F. et al., 2006, *A&A*, 448, L43
- Bignami G. F., Caraveo P. A., Mereghetti S., 1993, *Nat*, 361, 704
- Blondin J. M., Chevalier R. A., Frierson D. M., 2001, *ApJ*, 563, 806
- Bryden G., Beichman C. A., Rieke G. H., Stansberry J. A., Stapelfeldt K. R., Trilling D. E., Turner N. J., Wolszczan A., 2006, *ApJ*, 646, 1038
- Caraveo P. A., De Luca A., Mignani R. P., Bignami G. F., 2001, *ApJ*, 561, 930
- Caraveo P. A., Bignami G. F., De Luca A., Mereghetti S., Pellizzoni A., Mignani R., Tur A., Becker W., 2003, *Sci*, 301, 1345
- Caraveo P. A., De Luca A., Mereghetti S., Pellizzoni A., & Bignami G. F., 2004, *Sci*, 305, 376
- Chevalier R. A., 1989, *ApJ*, 346, 847
- de Luca A., Caraveo P. A., Mattana F., Pellizzoni A., Bignami G. F., 2006, *A&A*, 445, L9
- Dodson R., Legge D., Reynolds J. E., McCulloch P. M., 2003, *ApJ*, 596, 1137
- Dodson R., Lewis D., McConnell D., Deshpande A. A., 2003a, *MNRAS*, 343, 116
- Dullemond C. P., Monnier J. D., 2010, *ARA&A*, 48, 205
- Ekşi K. Y., Alpar M. A., 2005, *ApJ*, 620, 390
- Faherty J., Walter F. M., Anderson J., 2007, *Ap&SS*, 308, 225
- Farihi J., 2010, preprint (astro-ph/1010.6067)
- Foster R. S., Fischer J., 1996, *ApJ*, 460, 902
- Harding A. K., Strickman M. S., Gwinn C., Dodson R., Moffet D., McCulloch P., 2002, *ApJ*, 576, 376
- Helfand D. J., Gotthelf E. V., Halpern, J. P., 2001, *ApJ*, 556, 380
- Johnston S., Hobbs G., Vigeland S., Kramer M., Weisberg J. M., Lyne, A. G., 2005, *MNRAS*, 364, 1397
- Jones P. B., 2007, *MNRAS*, 382, 871
- Kaplan D. L., Chakrabarty D., Wang Z., Wachter S., 2009, *ApJ*, 700, 149
- Kargaltsev O. Y., Pavlov G. G., Zavlin V. E., Romani R. W., 2005, *ApJ*, 625, 307

- Konacki M., Wolszczan A., 2003, *ApJ*, 591, L147
- Malofeev V. M., Malov O. I., 1997, *Nat*, 389, 697
- Malofeev V. M., Malov O. I., Teplykh D. A., Tyul'Bashev S. A., Tyul'Basheva G. E., 2005, *Astronomy Reports*, 49, 242
- Malofeev V. M., Teplykh D. A., Malov O. I., 2010, *Astronomy Reports*, 54, 995
- Markwardt C. B., Ogelman H., 1995, *Nat*, 375, 40
- Martin C., Halpern J. P., Schiminovich D., 1998, *ApJ*, 494, L211
- Matttox J. R., Halpern J. P., Caraveo P. A., 1998, *ApJ*, 493, 891
- Melis C., Jura M., Albert L., Klein B., Zuckerman B., 2010, *ApJ*, 722, 1078
- Mignani R. P., De Luca A., Kargaltsev O., Pavlov G. G., Zaggia S., Caraveo P. A., Becker W., 2003, *ApJ*, 594, 419
- Mignani R. P., Zharikov S., Caraveo P. A., 2007, *A&A*, 473, 891
- Ng C.-Y., Romani R. W., 2008, *ApJ*, 673, 411
- Pavlov G. G., Zavlin V. E., Sanwal D., Burwitz V., Garmire G. P., 2001, *ApJ*, 552, L129
- Pavlov G. G., Kargaltsev O. Y., Sanwal D., Garmire G. P., 2001a, *ApJ*, 554, L189
- Pavlov G. G., Sanwal D., Zavlin V. E., 2006, *ApJ*, 643, 1146
- Pavlov G. G., Bhattacharyya S., Zavlin V. E., 2010, *ApJ*, 715, 66
- Pellizzoni A. et al., 2010, *Sci*, 327, 663
- Pellizzoni A., Govoni F., Esposito P., Murgia M., Possenti A., 2011, preprint (astro-ph/1102.4754)
- Perna R., Hernquist L., Narayan R., 2000, *ApJ*, 541, 344
- Rho J., Reach W. T., Tappe A., Hwang U., Slavin J. D., Kozasa T., Dunne L., 2009, *ApJ*, 700, 579
- Romani R. W., Kargaltsev O., Pavlov G. G., 2005, *ApJ*, 627, 383
- Salvati M., 2010, *A&A*, 513, A28
- Sandberg A., Sollerman J., 2009, *A&A*, 504, 525
- Serafimovich N., Shibarov Yu. A., Lundqvist P., Sollerman J., 2004, *A&A*, 425, 1041
- Shibarov Yu. A., Koptsevich A. B., Sollerman J., & Lundqvist P., 2003, *A&A*, 406, 645
- Shibarov Yu. A. et al., 2006, *A&A*, 448, 313
- Shibarov Yu. A., Lundqvist N., Lundqvist P., Sollerman J., Zyuzin D., 2008, *A&A*, 486, 273
- Shvartsman V. F., 1970, *SvA*, 14, 527
- Slane P., Helfand D. J., Reynolds S. P., Gaensler B. M., Lemiére A., Wang Z., 2008, *ApJ*, 676, L33
- Temim T. et al., 2009, *AJ*, 137, 5155
- Vrtilek S. D., Raymond J. C., Garcia M. R., Verbunt F., Hasinger G., Kurster M., 1990, *A&A*, 235, 162
- Wang Z., Chakrabarty D., Kaplan D. L., 2006, *Nat*, 440, 772
- Williams B. J. et al., 2008, *ApJ*, 687, 1054
- Wolszczan A., 1994, *Sci*, 264, 538
- Zharikov S. V., Shibarov Yu. A., Zyuzin D. A., Mennickent R. E., Komarova V. N., 2008, *A&A*, 492, 805
- Zyuzin D. A., Danilenko A. A., Zharikov S. V., Shibarov Yu. A., 2009, *A&A*, 508, 855